

Article

Improved Mechanical Properties of Biocompatible Zn-1.7%Mg and Zn1.7%Mg-0.2%Zr Alloys Deformed with High-Pressure Torsion

Natalia Martynenko ^{1,*}, Natalia Anisimova ^{1,2,3,*}, Natalia Tabachkova ^{4,5}, Georgy Rybalchenko ⁶, Igor Shchetinin ^{1,4}, Olga Rybalchenko ¹, Maria Shinkareva ^{1,3}, Dmitry Prosvirnin ¹, Elena Lukyanova ¹, Diana Temralieva ¹, Andrey Koltygin ⁷, Mikhail Kiselevskiy ^{2,3} and Sergey Dobatkin ¹

¹ A.A. Baikov Institute of Metallurgy and Materials Science of the Russian Academy of Sciences, Leninskiy Prospect, 49, 119334 Moscow, Russia; ingvar@misis.ru (I.S.); rybalch@mail.ru (O.R.); m.shinkareva29@mail.ru (M.S.); imetran@yandex.ru (D.P.); helenelukyanova@gmail.com (E.L.); diana4-64@mail.ru (D.T.); sdobatkin@imet.ac.ru (S.D.)

² N.N. Blokhin National Medical Research Center of Oncology (N.N. Blokhin NMRCO) of the Ministry of Health of the Russian Federation, Kashirskoye Highway, 23, 115478 Moscow, Russia; kisele@inbox.ru

³ Center for Biomedical Engineering, National University of Science and Technology "MISIS", Leninskiy Prospect, 4, 119049 Moscow, Russia

⁴ Department of Physical Materials Science, National University of Science and Technology "MISIS", Leninskiy Prospect, 4, 119049 Moscow, Russia; ntabachkova@gmail.com

⁵ A.M. Prokhorov General Physics Institute of the Russian Academia of Science, St. Vavilova, 38, 119333 Moscow, Russia

⁶ P.N. Lebedev Physical Institute of the Russian Academy of Sciences, Leninskiy Prospect, 53, 119991 Moscow, Russia; rybalchenkov@lebedev.ru

⁷ Department of Casting Technologies and Artistic Processing of Materials, National University of Science and Technology "MISIS", 119049 Moscow, Russia; misistlp@mail.ru

* Correspondence: nataliasmartynenko@gmail.com (N.M.); n_anisimova@list.ru (N.A.)



Citation: Martynenko, N.; Anisimova, N.; Tabachkova, N.; Rybalchenko, G.; Shchetinin, I.; Rybalchenko, O.; Shinkareva, M.; Prosvirnin, D.; Lukyanova, E.; Temralieva, D.; et al. Improved Mechanical Properties of Biocompatible Zn-1.7%Mg and Zn1.7%Mg-0.2%Zr Alloys Deformed with High-Pressure Torsion. *Metals* **2023**, *13*, 1817. <https://doi.org/10.3390/met13111817>

Academic Editors: Filippo Berto and Ricardo Branco

Received: 30 August 2023

Revised: 20 October 2023

Accepted: 25 October 2023

Published: 27 October 2023



Copyright: © 2023 by the authors. Licensee MDPI, Basel, Switzerland. This article is an open access article distributed under the terms and conditions of the Creative Commons Attribution (CC BY) license (<https://creativecommons.org/licenses/by/4.0/>).

Abstract: The potential medical Zn-1.7%Mg and Zn-1.7%Mg-0.2%Zr alloys strengthened using high-pressure torsion (HPT) were investigated in this work. HPT led to a significant refinement of the microstructure of both alloys with the formation of an ultrafine-grained structure (UFG). The average grain size after HPT was ~700–800 nm for both alloys. The formation of the UFG structure led to an increase in the ultimate tensile strength of up to 401 ± 16 and 482 ± 12 MPa for the Zn-1.7%Mg and Zn-1.7%Mg-0.2%Zr alloys, respectively. Additionally, a variation in ductility of the Zn-1.7%Mg and Zn-1.7%Mg-0.2%Zr alloys of up to $56.3 \pm 16.9\%$ and $4.4 \pm 0.6\%$, respectively, was also observed, apparently due to textural changes. HPT led to a small increase in the degradation rate of the alloys after 1 day of incubation in the medium. However, an increase in the incubation period of up to 30 days slowed down the degradation process and leveled the difference between the initial and HPT-treated state of the alloys. HPT did not affect the cytotoxicity of the Zn-1.7%Mg-0.2%Zr alloy and contributed to the reduction of hemolysis. Thus, the processing of the Zn-1.7%Mg and Zn-1.7%Mg-0.2%Zr alloys using HPT accelerated their biodegradation without compromising their biocompatibility.

Keywords: zinc alloys; high-pressure torsion; X-ray analysis; mechanical properties; corrosion resistance; biocompatibility in vitro

1. Introduction

In recent years, zinc alloys have become competitors with Mg and Fe-based alloys for creating bioresorbable implants due to their good biocompatibility and acceptable degradation rates [1–3]. Zinc is an essential trace element that promotes bone growth [4,5] and plays an important role in strengthening the human immune system [6]. Furthermore, zinc has been shown to suppress atherosclerosis [7], is necessary for protein synthesis [8], muscle

growth, and recovery [9], promotes wound healing [10], regulates hormone production [11], etc. Moreover, zinc ions are critical for cell growth and proliferation [12,13], including osteoblasts [14,15]. However, despite their numerous advantages, the main drawback of zinc alloys that limits their use as materials for bioresorbable implants (BRIs) is their low mechanical properties. For example, Li et al. reported that the tensile strength and ductility of pure cast zinc are only 18 MPa and 0.3%, respectively [16]. Tong et al. determined the ultimate tensile strength (UTS), yield stress (YS), and elongation (EL) as 33.6 MPa, 29.3 MPa, and 1.2%, respectively [17]. These values represent an improvement compared to the pure cast zinc mentioned earlier, but they still fall below the mechanical properties required for many biomedical implants. Alloying is a universal method for modifying the mechanical and corrosion properties of materials. By adding different alloying elements, it is possible to accelerate or slow down the corrosion process of zinc, as well as increase its strength. For example, Tong et al. conducted a systematic study on the influence of 0.2 at.% of various rare earth metals (REMs), namely Sc, Y, La, Ce, Pr, Nd, Sm, Eu, Gd, Tb, Dy, Ho, Er, Tm, Yb, and Lu, on the corrosion resistance and mechanical properties of pure Zn [18]. They demonstrated that Y had the greatest effect on the strength of pure zinc (UTS > 200 MPa), while the alloy with Tb showed the least strength improvement (UTS ~100 MPa). At the same time, all the investigated alloys showed degradation rates (DRs) in simulated body fluid (SBF) that were close to the DR of pure Zn (0.08–0.12 mm/year). However, it is important to consider not only the influence of the element on the corrosion and mechanical properties of zinc but also its biocompatibility when selecting the optimal alloying system. Indeed, there is currently a limited range of systems being considered for the development of biodegradable medical devices. The most extensively studied alloying elements for biodegradable medical devices include Mg [16,19], Li [20,21], Mn [21], Cu [21,22], Ca [16], Ag [23], Fe [24], Sr [16,25], and Zr [26]. These elements have a good effect on the strength, corrosion resistance, and biocompatibility of Zn. But often alloying does not improve the ductility of zinc and, in some cases, it may even worsen it. This makes it challenging to further utilize these alloys as materials for medical purposes.

One of the most effective methods for enhancing the strength and ductility of alloys is microstructure refinement. Microstructure refinement can be achieved using various methods, such as the addition of grain-refining elements during casting, plastic deformation, and recrystallization. The volume fraction of the grain boundaries increases, resulting in an enhancement of the strength and, in some cases, the ductility after refinement of the microstructure. For example, the addition of grain-refining modifiers involves the formation of solid particles into the melt during the pre-crystallization stage. These particles act as nucleation sites, promoting the formation of small and equiaxed grains during solidification. As a result, the microstructure is refined, leading to improved mechanical properties, including increased strength and sometimes ductility. One of the most popular grain-refining modifiers is Zr. It is used to refine the microstructure of many alloys, such as those based on Al [27] and Mg [28,29]. Zinc alloys are no exception. Li et al. demonstrated that adding 0.1 wt.% Zr to a Zn-4%Al (Further in the text, the composition of the alloys is indicated in wt.%, unless otherwise indicated) alloy significantly refines its microstructure due to the formation of Zr-containing particles [30]. A similar situation occurred in the Zn-1%Mg alloy with the addition of 0.1 and 0.2 wt.% Zr, where the formation of Zn₂₂Zr phase particles resulted in grain refinement [31]. However, the most effective method for enhancing mechanical properties is a combination of plastic deformation and the addition of grain-refining modifiers. In this case, along with improved strength, an increase in ductility occurs due to the formation of a favorable combination of microstructures and textures. For example, Watroba et al. showed that adding 0.05 wt.% Zr to a Zn-1%Ag alloy followed by extrusion at 250 °C results in a combination of strength and ductility, with values of 211 ± 1 MPa and 35 ± 1%, respectively [32]. Jin et al. demonstrated that the strength and elongation of hot-rolled Zn-1.5%Cu-1.0%Ag-xZr alloys initially increase and then decrease with an increasing Zr content [33]. This approach has also shown promise in obtaining high-strength alloys of the Zn-Mg-Zr system with various Mg and Zr contents [31,34,35].

Therefore, the aim of this study was to investigate the combined effect of adding 0.2 wt.% Zr and using high-pressure torsion (HPT) on the microstructure, mechanical properties, and biological activity of a Zn-1.7%Mg alloy. The work will evaluate the effect of HPT on the grain size of the alloys with and without the addition of zirconium. At the same time, the effect of the grain size of HPT-treated alloys on their corrosion resistance, and therefore biocompatibility, will also be investigated. The biological activity of the alloys was studied by estimating the hemolytic activity and cytotoxicity, allowing us to assess the biocompatibility of medical materials.

2. Materials and Methods

The effect of high-pressure torsion (HPT) on the microstructure, phase composition, texture, and mechanical and functional properties of Zn-1.7%Mg and Zn-1.7%Mg-0.2%Zr alloys was investigated in this study. The alloys were melted in an induction furnace without the use of a protective atmosphere following the procedure described in [36]. The actual composition of the obtained alloys was determined using a Bruker S8 Tiger sequential X-ray fluorescence wave-dispersive spectrometer (series 2; Bruker, Karlsruhe, Germany) according to the standard method provided by the manufacturer. The actual composition of the alloys was determined as Zn-1.69%Mg and Zn-1.66%Mg-0.226%Zr. The alloys were annealed at 320 °C for 20 h, followed by water quenching before HPT. Disks with a diameter of 20 mm and a thickness of 1.5 mm were used for high-pressure torsion. Deformation was carried out at room temperature and under a pressure of 6 GPa. The deformation speed was 1 revolution per minute.

The microstructure of the alloys in their initial states was examined using a JSM-7001F (JEOL, Tokyo, Japan) scanning electron microscope (SEM). For that purpose, the prepared samples were etched using a 0.5% HNO₃ solution in ethanol according to the standard procedure. The microstructure of the alloys was examined using a transmission electron microscope (TEM) JEM-2100 (JEOL, Tokyo, Japan) equipped with an energy-dispersive spectrometer (EDS). The samples for the investigation of the microstructure of the alloys after HPT were prepared using an electrochemical method and a Struers TenuPol-5 unit (Struers, Copenhagen, Denmark) at a voltage of 20 V. Image Expert Professional 3 software (version 3, Nexsys, Moscow, Russia) was used to calculate the average grain size of the alloys after HPT. A random section method was used to calculate the average grain size. For this purpose, at least 20 fields of view were used and at least 350 grains were measured. The results are presented as the mean value \pm standard deviation.

An Ultima IV X-ray diffractometer (Rigaku, Tokyo, Japan) using CuK α radiation and a graphite monochromator on a diffracted beam was used for X-ray diffraction (XRD) analysis. Phase analysis was performed using the PDXL2 software package (Rigaku, Tokyo, Japan) and the Powder Diffraction File (PDF2) database (ICDD, Newtown Square, PA, USA). The texture analysis was conducted using the method of constructing direct pole figures using a multifunctional attachment (Rigaku, Tokyo, Japan).

The degradation rate of the alloys before and after HPT was investigated using the standard method described in [37]. For these goals, the pre-polished samples in the form of 1/8 disks with a diameter of 20 mm and a thickness of 1 mm were sterilized in 70% ethanol for 2 h, and then dried under sterile conditions. The immersion tests were conducted at a temperature of 37 °C for 1 and 30 days in a complete growth medium based on Eagle's Minimum Essential Medium (Sigma, Welwyn Garden City, UK). A more detailed testing methodology, including sample cleaning of the degradation products and calculation of the average degradation rate, is described in [38]. The surface examinations of the samples after immersion tests and prior to the removal of the degradation products were performed using a JSM-7001F scanning electron microscope (JEOL, Tokyo, Japan).

The microhardness of the alloys was measured using a Vickers microhardness tester, in particular the 402MVD model from Instron Wolpert Wilson Instruments (Wilson Instruments, Norwood, MA, USA). The applied load during indentation was 100 g with a holding time of 10 s. The measurements were conducted on samples that were ground using P2500

abrasive paper and polished. Samples were securely and firmly fixed during testing. In the case of the initial alloys, the microhardness was measured at 10 different points on the sample surface, and then the averaged value was calculated. For the samples after HPT, the change in microhardness along the diameter of the sample with a step size of 1 mm was investigated. At each point, five measurements were taken to obtain the averaged value of microhardness. The mechanical properties of the alloys before and after HPT were measured on flat specimens (working length—5.75 mm, cross-section— 2×1 mm) using an Instron 3382 testing machine (Instron, High Wycombe, UK). In the case of the alloys after HPT, the samples were cut from the region corresponding to the half-radius of the disks [36].

Square-shaped samples with dimensions of 5 mm \times 5 mm \times 2 mm (length \times width \times thickness) were used for biological research. They were sterilized using immersion in 70% ethanol for 2 h, followed by air-drying under sterile conditions. The biological studies included the evaluation of the hemolytic and cytotoxic activities of the samples in relation to red blood cells (RBCs) and white blood cells (WBCs) isolated from Balb/c mice, in accordance with the previously described procedure [38].

To evaluate the hemolytic activity of the samples, the RBCs were suspended in Hank's solution (PanEco, Moscow, Russia) at a concentration of 4.42×10^6 cells per 1 mL and incubated with the samples for 2 h in a 5% carbon dioxide atmosphere at 37 °C. At the end of the incubation period, the RBC suspension was collected from each well and centrifuged at 3000 rpm for 5 min. Then, the optical density (OD) of the supernatant was measured in a 96 well plate (SPL Life Science, Geumgang-ro, Korea) at 540 nm using a Spark microplate reader (Tecan, Männedorf, Switzerland). As a 100% control, an RBC suspension treated with Triton X-100 (PanReac, AppliChem, Barcelona, Spain) was used. As a 0% control, a cell suspension that was incubated without any samples was used. The hemolysis results were calculated using the following formula [39]:

$$\text{Hemolysis (\%)} = \frac{OD (\text{Alloy}) - OD (0\% \text{ control})}{OD (100\% \text{ control}) - OD (0\% \text{ control})} \times 100$$

To evaluate the cytotoxic activity of the alloys, the WBCs were suspended in a complete growth medium at a concentration of 3×10^5 cells per mL and incubated with the alloy samples for 24 h at 37 °C in a 5% carbon dioxide atmosphere. Subsequently, the cellular activity of lactate dehydrogenase was measured and calculated using a Lactate Dehydrogenase Activity Assay Kit (Sigma-Aldrich, St. Louis, MO, USA) according to the manufacturer's instructions. The optical density measurements were performed in a 96 well plate at 450 nm using a microplate reader. As a control, the WBC suspension was incubated without any samples. The cell viability was assessed using the following formula:

$$\text{Cell viability (\%)} = \frac{OD (\text{Alloy}) - OD (\text{Cell medium})}{OD (\text{Control}) - OD (\text{Cell medium})} \times 100\%$$

Three samples of the same alloy state were used to assess the degradation rate and biocompatibility. The results are presented as the mean value \pm standard deviation. The statistical analysis was performed using Student's *t*-test. Differences were considered statistically significant at $p < 0.05$.

3. Results

The SEM images of the microstructure of the Zn-1.7%Mg and Zn-1.7%Mg-0.2%Zr alloys in their initial states are presented in Figure 1. The microstructure of both alloys consists of α -Zn grains with an average size of ~ 30 μm for the Zn-1.7%Mg alloy and ~ 15 μm for the Zn-1.7%Mg-0.2%Zr alloy. According to the SEM-EDS mapping data, a Mg-containing phase is observed surrounding these grains. In addition, an insignificant amount of Zr was also detected in the solid solution based on the α -Zn in the Zn-1.7%Mg-0.2%Zr alloy in its initial state (Figure 1b).

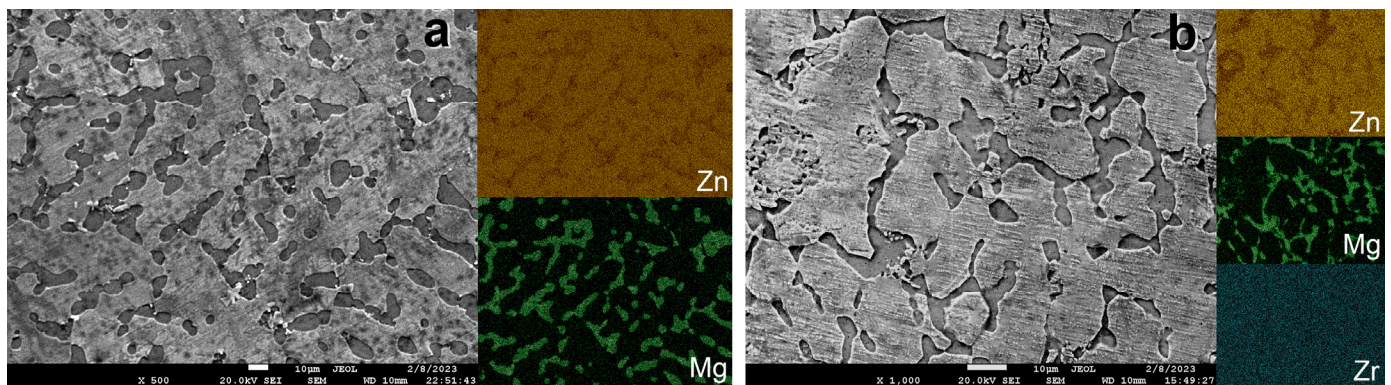


Figure 1. Microstructure of Zn-1.7%Mg (a) and Zn-1.7%Mg-0.2%Zr (b) alloys in their initial states.

A significant refinement of the dendritic α -Zn cells, resulting in the formation of an ultrafine-grained (UFG) microstructure, was observed after HPT (Figure 2). The microstructure of the Zn-1.7%Mg alloy after HPT consists of recrystallized α -Zn grains with an average size of 660 ± 20 nm. Additionally, it should be noted that the magnesium-rich phase also significantly refines after HPT. In this case, the formation of a nanostructure with a grain size of approximately 50–100 nm occurred. The precipitation of magnesium-rich particles with an average size of approximately 50 nm is also observed after HPT.

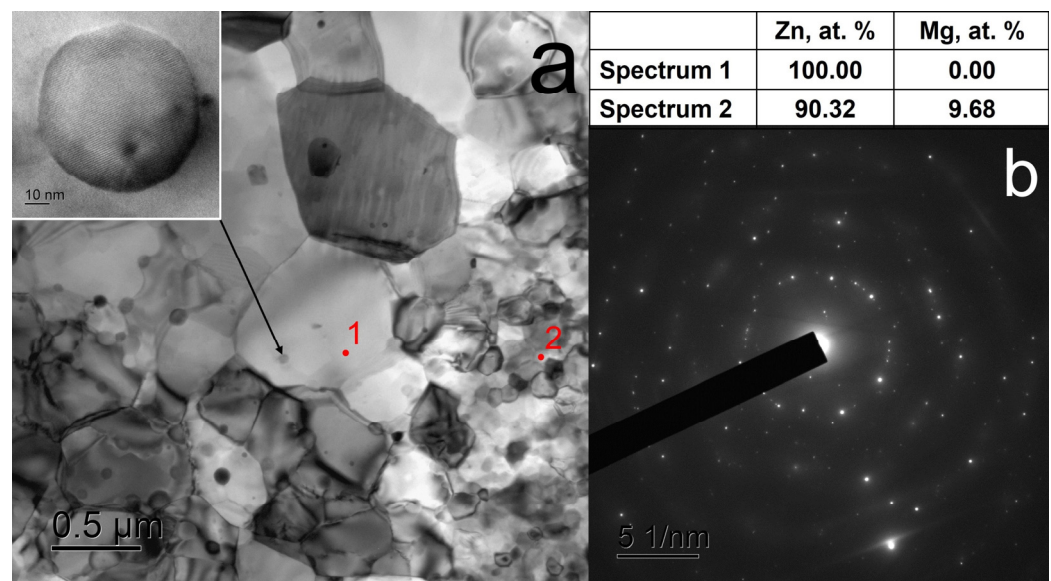


Figure 2. TEM images of microstructure of the Zn-1.7%Mg alloy after HPT (a) and its selected area electron diffraction pattern (b).

In the case of the Zn-1.7%Mg-0.2%Zr alloy, the microstructure is also significantly refined after HPT (Figure 3). However, in this case, the average grain size is 730 ± 40 nm. The magnesium-rich phase also significantly refines with the formation of grains with a size of about 50–100 nm occurring, but no particle precipitation was observed as in the Zn-1.7%Mg alloy. It is worth noting that in the case of the Zn-1.7%Mg-0.2%Zr alloy, extinction contours are observed along the grain boundaries, indicating the presence of significant internal stresses within them (Figure 3a).

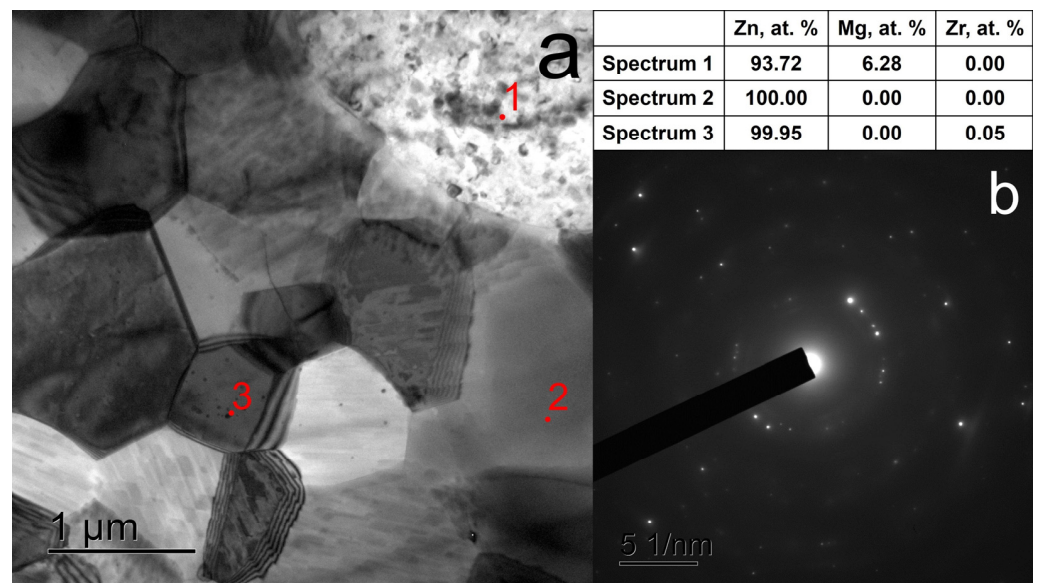


Figure 3. TEM images of microstructure of the Zn-1.7%Mg-0.2%Zr alloy after HPT (a) and its selected area electron diffraction pattern (b).

According to the phase analysis results (Figure 4, Table 1), the Zn-1.7%Mg alloy after annealing consisted of a mixture of an α -Zn phase ($P6_3/mmc$, card number 01-078-9363) and $MgZn_2$ phase ($P6_3/mmc$, card number 01-071-9623). The formation of the $MgZn_2$ phase can be attributed to the occurrence of non-equilibrium crystallization processes, which is confirmed by the SEM-EDS mapping data. HPT of the Zn-1.7%Mg alloy leads to grain refinement and the stimulation of diffusion processes, resulting in the formation of an equilibrium mixture of α -Zn and Mg_2Zn_{11} phases ($Pm\bar{3}$, card number 03-065-1853). It should be noted that a noticeable increase in the intensity of the (001) type lines in the diffraction pattern of the Zn-1.7%Mg alloy occurred after HPT, which may indicate the formation of a basal texture. In the Zn-1.7%Mg-0.2%Zr alloy, after annealing, the presence of an α -Zn phase ($P6_3/mmc$, card number 01-078-9363), Mg_2Zn_{11} phase ($Pm\bar{3}$, card number 03-065-1853), and $Zn_{22}Zr$ phase ($Fd\bar{3}m$, card number 01-072-3397) is observed. The absence of the $MgZn_2$ phase indicates a more equilibrium state being achieved after annealing. The presence of the $Zn_{22}Zr$ phase is not detected using phase analysis. However, it is noteworthy that after HPT, the lattice spacing of the Mg_2Zn_{11} phase in the Zn-1.7%Mg-0.2%Zr alloy is larger than that in the Zn-1.7%Mg alloy (Table 1). The increase in the lattice period of the Mg_2Zn_{11} phase may be attributed to the formation of a solid solution with Zr substitution in the $(Mg, Zr)_2Zn_{11}$ phase, as Zr has a larger atomic radius compared to Mg. A sharp increase in the intensity of the (001) type lines is also observed in the Zn-1.7%Mg-0.2%Zr alloy after HPT, which may indicate the formation of a basal texture.

Table 1. Result of XRD analysis of the Zn-1.7%Mg and Zn-1.7%Mg-0.2%Zr alloys.

Alloy	Phase Composition		Periods of the Phase Lattice ($\pm 0.002 \text{ \AA}$)
	Phase	Mass Fraction, wt. %	
Zn-1.7%Mg, annealing	Zn ($P6_3/mmc$)	92 ± 3	$a = 2.664 \text{ \AA}$, $c = 4.947 \text{ \AA}$
	$MgZn_2$ ($P6_3/mmc$)	8 ± 1	$a = 5.218 \text{ \AA}$, $c = 8.564 \text{ \AA}$
Zn-1.7%Mg, HPT	Zn ($P6_3/mmc$)	77 ± 3	$a = 2.663 \text{ \AA}$, $c = 4.942 \text{ \AA}$
	Mg_2Zn_{11} ($Pm\bar{3}$)	23 ± 1	$a = 8.533 \text{ \AA}$
	Zn ($P6_3/mmc$)	79 ± 4	$a = 2.665 \text{ \AA}$, $c = 4.948 \text{ \AA}$
Zn-1.7%Mg-0.2%Zr, annealing	Mg_2Zn_{11} ($Pm\bar{3}$)	20 ± 2	$a = 8.541 \text{ \AA}$
	$Zn_{22}Zr$ ($Fd\bar{3}m$)	1 ± 0.5	$a = 14.777 \text{ \AA}$
Zn-1.7%Mg-0.2%Zr, HPT	Zn ($P6_3/mmc$)	77 ± 3	$a = 2.665 \text{ \AA}$, $c = 4.946 \text{ \AA}$
	Mg_2Zn_{11} ($Fd\bar{3}m$)	23 ± 2	$a = 8.539 \text{ \AA}$

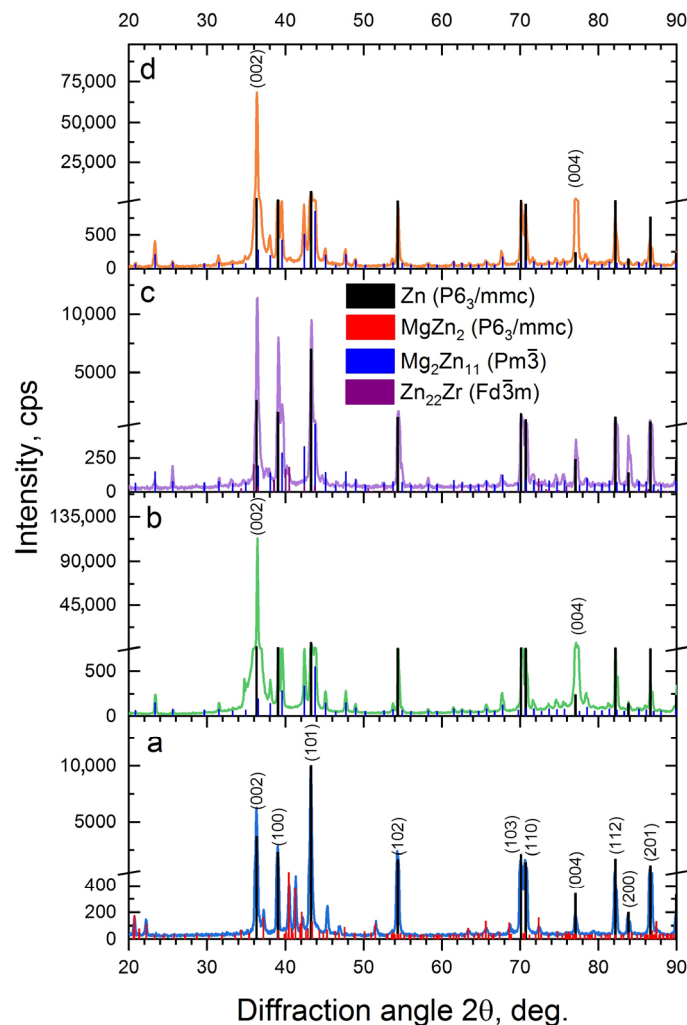


Figure 4. Results of XRD analysis of the Zn-1.7%Mg (a,b) and Zn-1.7%Mg-0.2%Zr (c,d) alloys in their initial states (a,c) and after HPT (b,d).

The pole figures (001) of the Zn-1.7%Mg and Zn-1.7%Mg-0.2%Zr alloys (Figure 5) confirm the presence of a sharp basal texture after HPT. The pole figures (001) of the Zn-1.7%Mg and Zn-1.7%Mg-0.2%Zr alloys showed that after annealing, this texture is not detected (Figure 5). A coarse grain effect is also observed in the Zn-1.7%Mg-0.2%Zr alloy (Figure 5c), which does not contradict the SEM data (Figure 1b). The pole figures (001) of the Zn-1.7%Mg and Zn-1.7%Mg-0.2%Zr alloys after deformation confirmed the formation of a basal texture; however, the texture axis deviates between the normal and the sample surface by an angle of no more than 5 degrees. HPT also leads to a significant increase in texture intensity, which is in good agreement with the results of XRD analysis. In addition, texture scattering is no longer observed in the HPT-treated alloys. The authors of this article previously showed a similar phenomenon in an HPT-treated Zn-1%Mg alloy [36]. At the same time, the intensity of the (001) lines of the deformed Zn-1.7%Mg-0.2%Zr alloy is slightly lower in comparison with the alloy without the addition of Zr ($\sim 1.1 \times 10^5$ cps for Zn-1.7%Mg vs. $\sim 7.5 \times 10^4$ cps for Zn-1.7%Mg-0.2%Zr; Figure 4d). The reason for this phenomenon may be the formation of Zn₂₂Zr particles. E.g., Zhao et al. in [40] showed that the particles of the Zn₂₂Zr phase can weaken texture and encourage pyramidal slip. The effect of texture weakening due to the presence of Zn₂₂Zr particles has also been demonstrated in Zn1AgxZr alloys [32].

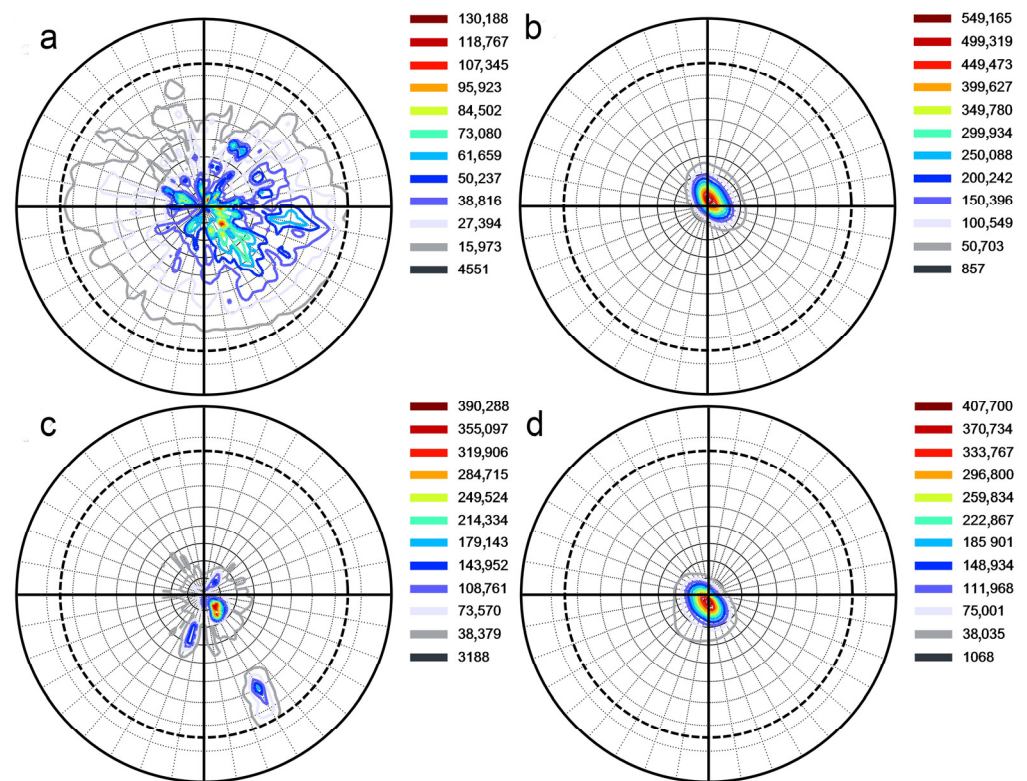


Figure 5. The texture of the Zn-1.7%Mg (a,b) and Zn-1.7%Mg-0.2% Zr (c,d) alloys in their initial states (a,c) and after high-pressure torsion (HPT) (b,d).

The investigation of the degradation processes of the alloys before and after HPT was conducted for 1 and 30 days (Figure 6). The study showed that the addition of 0.2% Zr does not lead to a significant deterioration in corrosion resistance. The degradation rate is 0.30 ± 0.03 and 0.33 ± 0.03 mm/year for the Zn-1.7%Mg and Zn-1.7%Mg-0.2%Zr alloys in their initial states after 1 day of incubation, respectively. After 30 days of incubation, the degradation rate decreases to 0.13 ± 0.04 and 0.11 ± 0.03 mm/year for the Zn-1.7%Mg and Zn-1.7%Mg-0.2%Zr alloys, respectively. HPT of both alloys leads to a significant acceleration of the degradation process during short-term tests. The degradation rate after 1 day of incubation in the growth medium is 0.45 ± 0.08 and 0.58 ± 0.13 mm/year for the HPT-treated Zn-1.7%Mg and Zn-1.7%Mg-0.2%Zr alloys, respectively. However, an increase in the incubation period results in a slowing down of the degradation process of both alloys. After 30 days of incubation in a complete growth medium, the degradation rate of the HPT-treated Zn-1.7%Mg alloy was 0.16 ± 0.02 mm/year, which is not significantly different from the degradation rate of the initial alloy (0.13 ± 0.04 mm/year). For the HPT-treated Zn-1.7%Mg-0.2%Zr alloy, the degradation rate after 30 days of incubation was 0.23 ± 0.04 mm/year, compared to 0.11 ± 0.03 mm/year in its initial state.

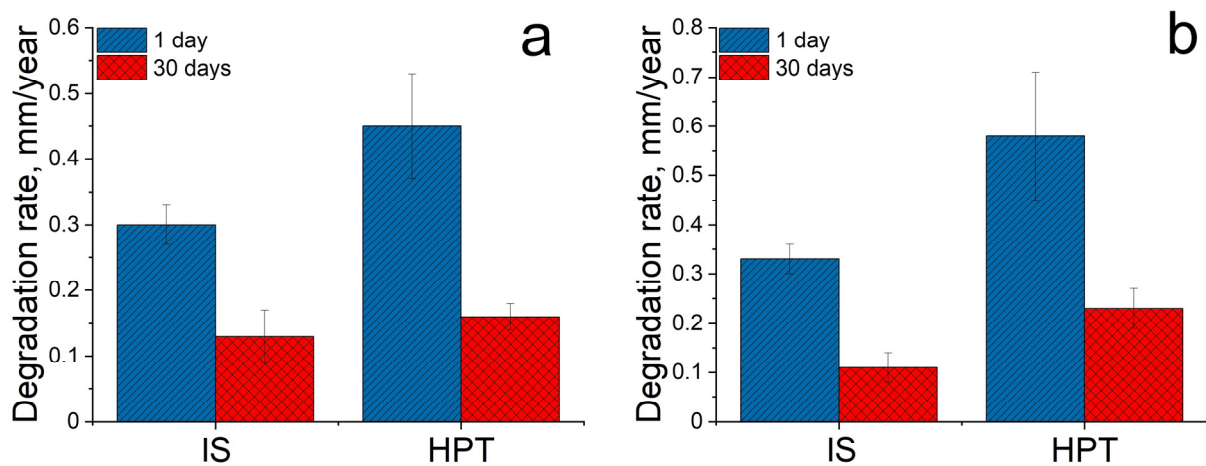


Figure 6. The degradation rate in mm/year for the Zn-1.7%Mg (a) and Zn-1.7%Mg-0.2%Zr (b) alloys before and after HPT.

Figure 7 shows the results of the surface examination of the Zn-1.7%Mg and Zn-1.7%Mg-0.2%Zr alloy samples in the initial and HPT-treated states after 30 days of incubation in a complete growth medium. The results showed that the degradation of the alloys is accompanied by the formation of a film consisting of degradation products. In the case of HPT-treated alloys, this film appears visually denser (Figure 7b,d).

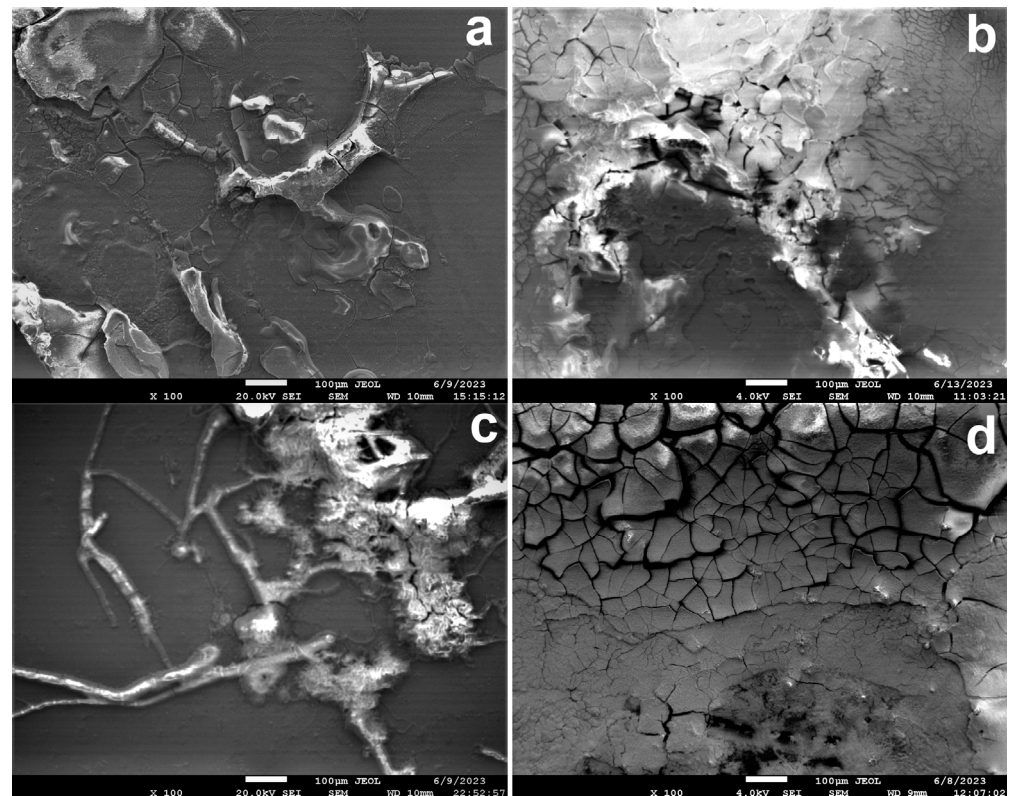


Figure 7. The surface of the Zn-1.7%Mg (a,b) and Zn-1.7%Mg-0.2%Zr (c,d) alloy samples before (a,c) and after HPT (b,d) after immersion tests.

Figure 8 shows the results of the microhardness study of the alloys before and after HPT. It should be noted that the addition of Zr results in an increase in the microhardness of the Zn-1.7%Mg alloy in its initial state from 1003 ± 42 to 1183 ± 42 MPa. HPT leads to an increase in the microhardness of the Zn-1.7%Mg alloy, while it has a weak influence on

the microhardness of the Zn-1.7%Mg-0.2%Zr alloy. It should be noted that the microhardness in the center of the HPT-treated alloy samples is lower than at half the radius. The inhomogeneity is caused by the uneven distribution of stresses during the HPT process of the samples. Typically, the maximum stresses occur at the periphery of the samples during the HPT process. As a result, the highest deformation of the samples occurs in this region. In our case, the microhardness of the HPT-treated alloy becomes homogeneous at a distance of 2 mm from the center of the disk. Comparing the microhardness of the HPT-treated alloys revealed that the alloy with the addition of Zr exhibits significantly higher microhardness compared to the similar alloy without Zr.

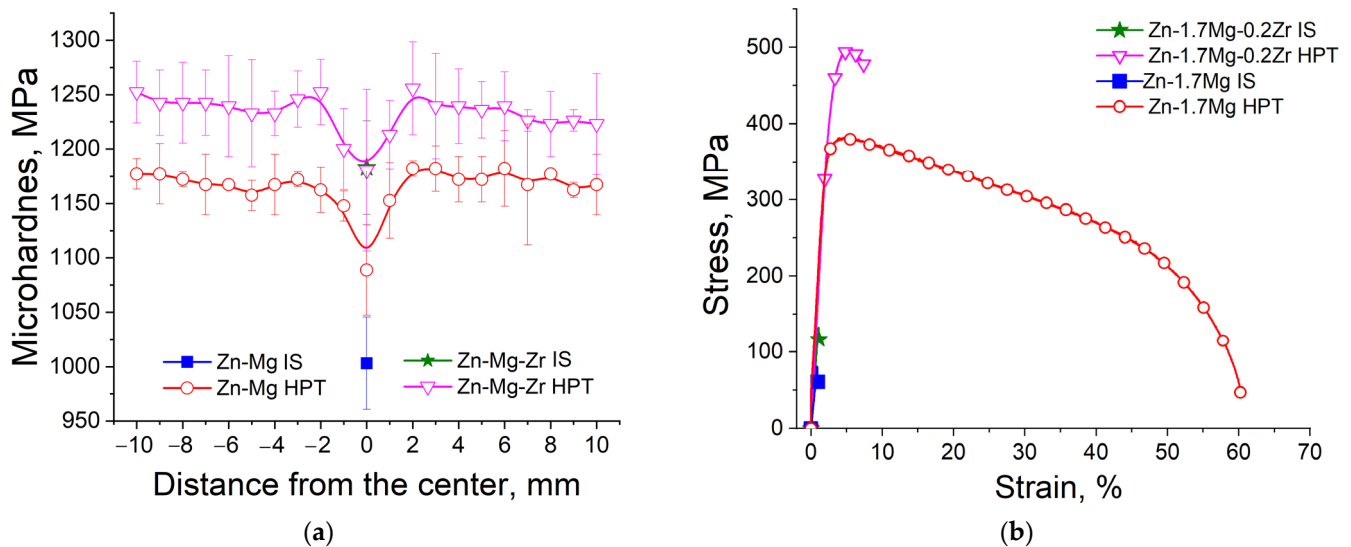


Figure 8. Distribution of microhardness over the diameter of the sample after HPT in comparison with initial microhardness value (a) and stress–strain curves (b) of the Zn-1.7%Mg and Zn-1.7%Mg-0.2%Zr alloys.

The results of the mechanical properties' investigation are presented in Figure 8 b and in Table 2. It should be noted that the addition of Zr leads to a significant increase in the yield strength of the Zn-1.7%Mg alloy and a slight improvement in the ultimate tensile strength. The refinement of the microstructure leads to an increase in the strength of the alloys by more than 5 times for the Zn-1.7%Mg alloy and by more than 3.5 times for the Zn-1.7%Mg-0.2%Zr alloy. The yield stress (YS) and ultimate tensile strength (UTS) of the Zn-1.7%Mg alloy increased from 47 ± 11 and 75 ± 14 MPa to 373 ± 15 and 401 ± 16 MPa, respectively. In the case of the Zn-1.7%Mg-0.2%Zr alloy, these values increased from 125 ± 7 and 128 ± 8 MPa to 376 ± 21 and 482 ± 12 MPa, respectively. Additionally, the increase in ductility (El) of the alloys after HPT should be noted. In the case of the Zn-1.7%Mg-0.2%Zr alloy, a ten-fold increase in ductility was observed (from $0.4 \pm 0.2\%$ to $4.4 \pm 0.6\%$). In the case of the Zn-1.7%Mg alloy, an increase in ductility of nearly 50 times (from $1.3 \pm 0.3\%$ to $56.3 \pm 16.9\%$) after HPT occurred.

Table 2. Mechanical properties of the Zn-1.7%Mg and Zn-1.7%Mg-0.2%Zr alloys in their initial states and after HPT.

Alloy	State	YS, MPa	UTS, MPa	El, %
Zn-1.7%Mg	Initial state	47 ± 11	75 ± 14	1.3 ± 0.3
	HPT	373 ± 15	401 ± 16	56.3 ± 16.9
Zn-1.7%Mg-0.2%Zr	Initial state	125 ± 7	128 ± 8	0.4 ± 0.2
	HPT	376 ± 21	482 ± 12	4.4 ± 0.6

To evaluate the effect of HPT on the biocompatibility of the alloys, their hemolytic activity and cytotoxicity were assessed. The studied HPT-treated alloys were characterized by good biocompatibility, while they did not affect the viability of the white blood cells and had low hemolytic activity, not exceeding an average of 5% (Figure 9). Comparative statistical analysis did not reveal significant differences in the level of hemolysis and cell viability after incubation with the Zn-1.7%Mg and Zn-1.7%Mg-0.2%Zr alloys in their initial states compared to with these alloys after HPT ($p > 0.05$). The absence of statistically significant differences in the biological properties of alloys with different elemental compositions should be also noted. However, a tendency for the hemolysis levels to decrease after incubation of the cells with the HPT-treated alloy samples was observed. This indicates an improvement in their biocompatibility compared to the initial state.

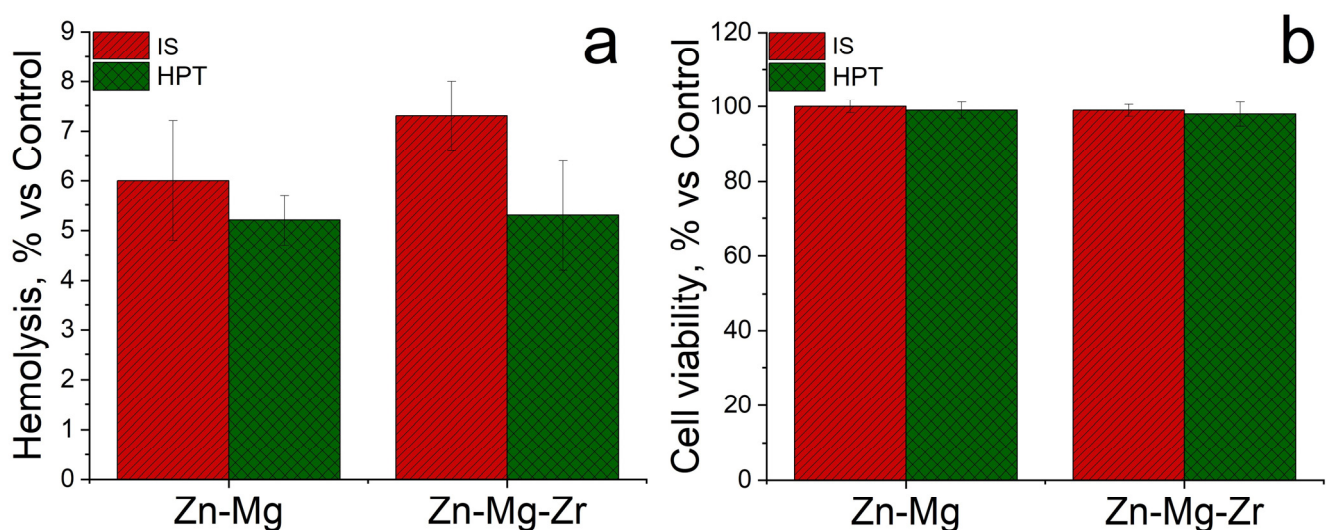


Figure 9. Hemolytic activity (a) and cell viability (b) of Zn-1.7%Mg and Zn-1.7%Mg-0.2%Zr alloys in the annealing state and after HPT.

4. Discussion

The conducted research has shown that HPT and the addition of Zr can significantly improve the strength and ductility of the Zn-1.7%Mg alloy. The addition of 0.2%Zr leads to a reduction in the grain size of α -Zn by approximately half (from 30 to 15 μm), which results in a significant increase in the YS (from 47 ± 11 MPa to 125 ± 7 MPa) and UTS (from 75 ± 14 MPa to 128 ± 8 MPa) of the alloy compared to in its initial state. Grain refinement is believed to be associated with the formation of Zn_{22}Zr particles in the Zn-1.7%Mg-0.2%Zr alloy. A similar effect was previously observed by Zhou et al. in their study [31]. Zhou et al. demonstrated that Zn_{22}Zr particles precipitate in the eutectic area, acting as nucleation centers for Zn dendrites [31]. This leads to a reduction in their size, thereby refining the microstructure. A similar effect, observed in pure Zn, was reported in [41]. HPT also leads to a further increase in the strength of both investigated alloys due to the formation of a hybrid structure consisting of ultra-fine α -Zn grains and nano-sized precipitates of the magnesium-containing phase. In our case, the presence of predominantly point reflections in the ring electron diffraction pattern indicates the formation of a microstructure with a high-angle misorientation of grains. Dynamic recrystallization may be one of the probable reasons for this. Bednarczyk et al. previously observed a similar effect in a HPT-treated Zn-0.5Cu alloy (wt.%) [22]. It should be noted that the HPT-treated alloy with 0.2%Zr exhibits a significantly higher strength compared to the Zn-1.7%Mg alloy, despite the minor differences in the microstructure size. The presence of $(\text{Mg}, \text{Zr})_2\text{Zn}_{11}$ particles likely causes this effect.

It is also worth noting that HPT leads to an increase not only in strength. In the case of the Zn-1.7%Mg-0.2%Zr alloy, an approximately 10-fold increase in ductility (from

0.4 ± 0.2% in the initial state to 4.4 ± 0.6% after HPT) is observed. In the case of the Zn-1.7%Mg alloy, the ductility also increased by about 10 times, but the ductility of the alloy after HPT was significantly higher in comparison with the HPT-treated Zn-1.7%Mg-0.2%Zr alloy (56.3 ± 16.9%). The probable reason for this effect is the texture changes after HPT. In our case, HPT of both alloys results in the formation of a strong basal texture. A similar texture was formed in the Zn-0.5Cu alloy processed using high-pressure torsion, which also led to a significant increase in ductility [22]. A notable enhancement in ductility is also observed in Mg-based alloys where a basal texture is formed after deformation [42–44]. The presence of fine-dispersed (Mg, Zr)₂Zn₁₁ particles in the Zn-1.7%Mg-0.2%Zr alloy after HPT can hinder the improvement of ductility during deformation. A comparison of the mechanical properties obtained in this study with the properties presented in the literature is shown in Table 3.

Table 3. Mechanical properties of Zn-Mg and Zn-Mg-Zr alloys after various deformation treatments.

System	Alloy	Treatment	YS, MPa	UTS, MPa	EL, %	Ref.
Zn-Mg	Zn-1.7%Mg	HPT at room temperature	373 ± 15	401 ± 16	56.3 ± 16.9	This study
	Zn-1.5%Mg	Room temperature rolling	-	366 ± 3.7	18.4 ± 2.0	[45]
	Zn-1.5%Mg	Extrusion at 300 °C	308 ± 34	333 ± 19	0.2 ± 0.1	[46]
	Zn-1.6%Mg	Rapid solidification + extrusion at 300 °C	332	370	9	[47]
	Zn-2%Mg	Extrusion at 400 °C	-	~380	~6	[48]
	Zn-1.6%Mg	ECAP at 150 °C (N = 12)	361	423	5.2	[49]
	Zn-1.6%Mg	ECAP at 150 °C (N = 8)	-	474	7	[50]
	Zn-1.7%Mg-0.2%Zr	HPT at room temperature	376 ± 21	482 ± 12	4.4 ± 0.6	This study
Zn-Mg-Zr	Zn-1%Mg-0.1%Zr	Extrusion at 280 °C	-	~332	~3.3	[31]
	Zn-1%Mg-0.2%Zr		-	~322	~3.3	
	Zn-1%Mg-0.02%Zr	Hot rolling	217.6 ± 2.0	259.6 ± 2.1	12.4 ± 1.3	[34]
	Zn-1%Mg-0.05%Zr		218.0 ± 2.1	263.2 ± 2.3	12.1 ± 1.1	
	Zn-1%Mg-0.1%Zr		219.1 ± 1.5	267.8 ± 1.8	10.7 ± 1.4	
	Zn-1%Mg-0.3%Zr		201.9 ± 2.5	266.1 ± 2.7	8.3 ± 1.1	
	Zn-0.5%Mg-0.5%Zr	Extrusion at 145 ± 15 °C	-	~300	-	[35]
	Zn-1%Mg-0.5%Zr		-	~360	-	
	Zn-1.5%Mg-0.5%Zr		-	~420	-	
	Zn-1%Mg-0.1%Zr	Extrusion at 145 °C	248	314	2.5	[40]
	Zn-1%Mg-0.25%Zr		236	300	2.5	
Zn-1%Mg-0.4%Zr	241		316	4.7		

The results of the current mechanical study significantly exceed the values reported for the Zn-(1.5–2)%Mg alloys processed using extrusion and rolling [45–48]. The strength of the alloys in the mentioned works does not exceed approximately 380 MPa, while the maximum achieved ductility is around 20%. At the same time, using ECAP achieves a strength level that exceeds that of the Zn-1.7%Mg alloy after HPT. However, the ductility of these alloys was significantly lower [49,50]. In the case of the Zn-1.7%Mg-0.2%Zr alloy, a unique combination of properties was achieved using the methods of HPT, including excellent strength (482 ± 12 MPa) and acceptable ductility (4.4 ± 0.6%). The strength and ductility obtained in similar alloys after extrusion at different temperatures are lower than the results obtained in this study [31,35,40]. A higher level of ductility was obtained for Zn-1%Mg-(0.02–0.3)%Zr alloys after hot rolling (up to 12.4 ± 1.3%). However, the strength values of the alloys in [34] were lower by almost half compared to the results obtained in this work.

The study of the corrosion resistance of the alloys revealed that HPT leads to an acceleration of the degradation processes. The degradation rate of the HPT-treated alloys after 1 day of incubation exceeds that of the initial alloys by approximately 50%. The increased degradation rate is caused by structural and phase changes and an increase in the density of defects in the crystalline lattice after deformation. For example, a significant increase in the Mg-containing phase is observed in the Zn-1.7%Mg alloy after HPT. This

can adversely affect its corrosion resistance by creating galvanic couples with the Zn matrix. Kafri et al. showed that the degradation rate of the Zn-1.3%Fe alloy increases due to microgalvanic corrosion between the zinc matrix and the Zn₁₁Fe phase particles [51]. In Zn-0.5Al-xMg alloys (x = 0–1%), an increase in Mg content of up to 1%, and consequently, the mass fraction of the Mg₂Zn₁₁ phase, leads to a decrease in corrosion resistance due to galvanic corrosion between the Zn and Mg₂Zn₁₁ phases [52]. At the same time, the presence of strong internal stress fields in the structure of the Zn-1.7%Mg-0.2%Zr alloy after HPT can also contribute to an increase in the degradation rate. Chen et al. demonstrated that an increase in the applied load accelerates the degradation rate of stents made from the magnesium WE43 alloy, iron, and zinc [53]. Wei et al. showed a similar effect of deformation on the corrosion resistance of zinc-based alloys [54]. At the same time, an increase in the incubation period of the alloys in the growth medium results in a significant reduction in the degradation rate due to the formation of a film composed of degradation products (Figure 7). It was demonstrated in [55] that the degradation of Zn-Mg alloys proceeds in three stages: activation of the surface, active corrosion, and passivation by the corrosion products. It also shown that the finer the microstructure of the alloy, the greater its effect on the formation of the passivation film [55]. In our case, the effect of an ultrafine-grained structure is more pronounced for the Zn-1.7%Mg alloy. Here, an increase in the incubation period of up to 30 days reduces the degradation rate of the initial and HPT-treated alloys by 2.3 and 2.8 times, respectively. In the case of the Zn-1.7%Mg-0.2%Zr alloy, a more pronounced corrosion rate reduction is observed for the alloy in its initial state (3 and 2.5 times over for the alloys before and after HPT, respectively). At the same time, the formation of a sharp basal texture, which is observed in HPT-treated alloys, usually improves the corrosion resistance of metals. For example, it was shown for pure Mg [56] and AZ31 [57] alloy that the (0001) basal plane has improved corrosion resistance. A similar situation was also observed in the deformed alloy Zn-2.03wt.%Cu-0.54wt.%Mn [58]. However, the increase in the degradation rate of the HPT-treated Zn-1.7%Mg and Zn-1.7%Mg-0.2%Zr alloys, in which a sharp basal texture is formed, indicates the prevailing influence of the microstructure in comparison with texture.

The changes in the microstructure of the alloys after HPT did not cause significant changes in the biological properties that characterize biocompatibility. There were no indications of increased cytotoxic effects due to contact with the Zn-1.7%Mg and Zn-1.7%Mg-0.2%Zr alloy samples after deformation treatment, despite the acceleration of degradation. It is noted in several studies that the acceleration of biodegradation in metals can lead to a deterioration in biocompatibility [59–61]. In particular, the authors observed a similar correlation during investigation of the magnesium WE43 alloy in their previous studies [62]. However, on the contrary, a slight decrease in the level of hemolysis was observed in this study, although this effect in the Zn-1.7%Mg alloy was not statistically significant. This effect may be associated with a favorable concentration of Zn ions in the growth medium. It was shown in previous studies that low concentrations of Zn²⁺ ions can improve cell viability, proliferation, and adhesion, while high concentrations of Zn²⁺ ions having the opposite effect [63–65]. It is possible that we would observe a more pronounced positive effect of the HPT-treated alloys on the preservation of the integrity and viability of the blood cells by varying the contact time between the alloys and the cells. This hypothesis will be investigated in our future studies. In general, the obtained data indicate that the mechanical processing of alloys based on a Zn-Mg system can significantly alter their mechanical properties without impairing their biocompatibility. This approach enables the creation of materials that are specifically dedicated to the fabrication of orthopedic implants, providing enhanced mechanical properties, biocompatibility, and corrosion resistance. These materials can address various challenges in modern medicine, including improving patient outcomes, reducing implant failure rates, and promoting tissue integration. This advancement ultimately contributes to the advancement of orthopedic surgery and medical technologies in general.

5. Conclusions

1. HPT results in the formation of ultrafine-grained structure in the Zn-1.7%Mg and Zn-1.7%Mg-0.2%Zr alloys, with grain sizes of 660 ± 20 nm and 730 ± 40 nm, respectively. Additionally, it leads to the formation of a nanoscale structure (50–100 nm) in the boundary phase. HPT also leads to the transformation of the MgZn₂ phase into a more thermodynamically stable phase Mg₂Zn₁₁ and increases its mass fraction in the Zn-1.7%Mg alloy. In the Zn-1.7%Mg-0.2%Zr alloy, HPT promotes the dissolution of the Zn₂₂Zr phase and the formation of the (Mg, Zr)₂Zn₁₁ phase.
2. HPT causes the formation of a sharp basal texture in both of the investigated alloys.
3. HPT accelerates the degradation process of both investigated alloys due to the structural and phase transformations that occur during deformation. At the same time, an increase in the incubation time slows down the degradation process due to the formation of a protective film.
4. The structural and textural changes caused by HPT result in a significant increase in the strength and ductility of both alloys. The strength of the Zn-1.7%Mg alloy after HPT was 401 ± 16 MPa, with a level of ductility of $56.3 \pm 16.9\%$. The strength and ductility of the Zn-1.7%Mg-0.2%Zr alloy after HPT was 482 ± 12 MPa and $4.4 \pm 0.6\%$, respectively.
5. HPT does not affect the cytotoxicity of the Zn-1.7%Mg-0.2%Zr alloy and contributes to a reduction in hemolysis.

Author Contributions: Conceptualization: N.M. and N.A.; methodology: M.K., A.K. and S.D.; software: N.M., N.A., N.T., G.R., I.S., O.R., M.S., D.P. and D.T.; validation: M.K. and S.D.; formal analysis: N.M. and N.A.; investigation: N.M., N.A., N.T., G.R., I.S., O.R., M.S., D.P., E.L. and D.T.; resources: G.R., A.K., M.K. and S.D.; data curation: S.D. and M.K.; writing—original draft preparation: N.M. and N.A.; writing—review and editing: N.M., N.A., G.R., O.R. and E.L.; visualization: N.M. and N.A.; supervision: M.K. and S.D.; project administration: S.D.; funding acquisition: S.D. All authors have read and agreed to the published version of the manuscript.

Funding: This research was supported by the Russian Science Foundation (Grant #22-23-00097).

Data Availability Statement: All the data required to reproduce these experiments are present in the article.

Acknowledgments: The study of the initial microstructure and surfaces of the samples after corrosion tests was undertaken using research equipment from the Shared Facility Centre at the Lebedev Physical Institute of the Russian Academy of Sciences.

Conflicts of Interest: The authors declare no conflict of interest.

References

1. Bandyopadhyay, A.; Mitra, I.; Goodman, S.B.; Kumar, M.; Bose, S. Improving biocompatibility for next generation of metallic implants. *Prog. Mater. Sci.* **2023**, *133*, 101053. [[CrossRef](#)] [[PubMed](#)]
2. Yuan, W.; Xia, D.; Wu, S.; Zheng, Y.; Guan, Z.; Rau, J.V. A review on current research status of the surface modification of Zn-based biodegradable metals. *Bioact. Mater.* **2022**, *7*, 192–216. [[CrossRef](#)] [[PubMed](#)]
3. Mostaed, E.; Sikora-Jasinska, M.; Drelich, J.W.; Vedani, M. Zinc-based alloys for degradable vascular stent applications. *Acta Biomater.* **2018**, *71*, 1–23. [[CrossRef](#)]
4. O'Connor, J.P.; Kanjilal, D.; Teitelbaum, M.; Lin, S.S.; Cottrell, J.A. Zinc as a Therapeutic Agent in Bone Regeneration. *Materials* **2020**, *13*, 2211. [[CrossRef](#)]
5. Yamaguchi, M. Role of nutritional zinc in the prevention of osteoporosis. *Mol. Cell Biochem.* **2010**, *338*, 241–254. [[CrossRef](#)]
6. Haase, H.; Rink, L. Zinc signals and immune function. *Biofactors* **2014**, *40*, 27–40. [[CrossRef](#)] [[PubMed](#)]
7. Shen, T.; Zhao, Q.; Luo, Y.; Wang, T. Investigating the Role of Zinc in Atherosclerosis: A Review. *Biomolecules* **2022**, *12*, 1358. [[CrossRef](#)]
8. Kimball, S.R.; Chen, S.J.; Risica, R.; Jefferson, L.S.; Leure-duPree, A.E. Effects of zinc deficiency on protein synthesis and expression of specific mRNAs in rat liver. *Metabolism* **1995**, *44*, 126–133. [[CrossRef](#)] [[PubMed](#)]
9. Hernández-Camacho, J.D.; Vicente-García, C.; Parsons, D.S.; Navas-Enamoradoc, I. Zinc at the crossroads of exercise and proteostasis. *Redox Biol.* **2020**, *35*, 101529. [[CrossRef](#)]

10. Lin, P.-H.; Sermersheim, M.; Li, H.; Lee, P.H.U.; Steinberg, S.M.; Ma, J. Zinc in Wound Healing Modulation. *Nutrients* **2018**, *10*, 16. [[CrossRef](#)]
11. Baltaci, A.K.; Mogulkoc, R.; Baltaci, S.B. Review: The role of zinc in the endocrine system. *Pak. J. Pharm. Sci.* **2019**, *32*, 231–239. [[PubMed](#)]
12. MacDonald, R.S. The Role of Zinc in Growth and Cell Proliferation. *J. Nutr.* **2000**, *130*, 1500S–1508S. [[CrossRef](#)] [[PubMed](#)]
13. Beyersmann, D.; Haase, H. Functions of zinc in signaling, proliferation and differentiation of mammalian cells. *Biometals* **2001**, *14*, 331–341. [[CrossRef](#)] [[PubMed](#)]
14. Seo, H.-J.; Cho, Y.-E.; Kim, T.; Shin, H.-I.; Kwun, I.-S. Zinc may increase bone formation through stimulating cell proliferation, alkaline phosphatase activity and collagen synthesis in osteoblastic MC3T3-E1 cells. *Nutr. Res. Pract.* **2010**, *4*, 356–361. [[CrossRef](#)]
15. Yusa, K.; Yamamoto, O.; Iino, M.; Takano, H.; Fukuda, M.; Qiao, Z.; Sugiyama, T. Eluted zinc ions stimulate osteoblast differentiation and mineralization in human dental pulp stem cells for bone tissue engineering. *Arch. Oral Biol.* **2016**, *71*, 162–169. [[CrossRef](#)]
16. Li, H.F.; Xie, X.H.; Zheng, Y.F.; Cong, Y.; Zhou, F.Y.; Qiu, K.J.; Wang, X.; Chen, S.H.; Huang, L.; Tian, L.; et al. Development of biodegradable Zn-1X binary alloys with nutrient alloying elements Mg, Ca and Sr. *Sci. Rep.* **2015**, *5*, 10719. [[CrossRef](#)]
17. Tong, X.; Zhang, D.; Zhang, X.; Su, Y.; Shi, Z.; Wang, K.; Lin, J.; Li, Y.; Lin, J.; Wen, C. Microstructure, mechanical properties, biocompatibility, and in vitro corrosion and degradation behavior of a new Zn-5Ge alloy for biodegradable implant materials. *Acta Biomater.* **2018**, *82*, 197–204. [[CrossRef](#)]
18. Du, S.; Shen, Y.; Zheng, Y.; Cheng, Y.; Xu, X.; Chen, D.; Xia, D. Systematic in vitro and in vivo study on biodegradable binary Zn-0.2 at% Rare Earth alloys (Zn-RE: Sc, Y, La–Nd, Sm–Lu). *Bioact. Mater.* **2023**, *24*, 507–523. [[CrossRef](#)]
19. Li, R.; Ding, Y.; Zhang, H.; Lei, J.; Shen, Y. Effective strengthening and toughening in Zn-1Mg alloy with bimodal grain structure achieved by conventional extrusion. *Mater. Sci. Eng. A* **2022**, *854*, 143850. [[CrossRef](#)]
20. Wang, M.; Yang, L.; Zhu, X.; Yang, L.; Shen, J.; Lu, T.; Liu, H.; Song, Z. Corrosion Mechanisms of a Biodegradable Zn-0.4Li Alloy in Simulated Gastrointestinal Environment. *Coatings* **2023**, *13*, 529. [[CrossRef](#)]
21. Yin, Y.-X.; Zhou, C.; Shi, Y.-P.; Shi, Z.-Z.; Lu, T.-H.; Hao, Y.; Liu, C.-H.; Wang, X.; Zhang, H.-J.; Wang, L.-N. Hemocompatibility of biodegradable Zn-0.8wt% (Cu, Mn, Li) alloys. *Mater. Sci. Eng. C* **2019**, *104*, 109896. [[CrossRef](#)] [[PubMed](#)]
22. Bednarczyk, W.; Kawałko, J.; Wątroba, M.; Gao, N.; Starink, M.J.; Bała, P.; Langdon, T.G. Microstructure and mechanical properties of a Zn-0.5Cu alloy processed by high-pressure torsion. *Mater. Sci. Eng. A* **2020**, *776*, 139047. [[CrossRef](#)]
23. Heiss, A.; Thatikonda, V.S.; Richter, A.; Schmitt, L.-Y.; Park, D.; Klotz, U.E. Development, Processing and Aging of Novel Zn-Ag-Cu Based Biodegradable Alloys. *Materials* **2023**, *16*, 3198. [[CrossRef](#)] [[PubMed](#)]
24. Shi, Z.-Z.; Gao, X.-X.; Chen, H.-T.; Liu, X.-F.; Li, A.; Zhang, H.-J.; Wang, L.-N. Enhancement in mechanical and corrosion resistance properties of a biodegradable Zn-Fe alloy through second phase refinement. *Mater. Sci. Eng. C* **2020**, *116*, 111197. [[CrossRef](#)]
25. Su, Y.; Fu, J.; Du, S.; Georgas, E.; Qin, Y.-X.; Zheng, Y.; Wang, Y.; Zhu, D. Biodegradable Zn-Sr alloys with enhanced mechanical and biocompatibility for biomedical applications. *Smart Mater. Med.* **2022**, *3*, 117–127. [[CrossRef](#)]
26. Wang, Z.; Zhang, Q.; Guo, P.; Gao, X.; Yang, L.; Song, Z. Effects of laser surface remelting on microstructure and properties of biodegradable Zn-Zr alloy. *Mater. Lett.* **2018**, *226*, 52–54. [[CrossRef](#)]
27. Ebrahimi, S.H.S.; Emamy, M.; Pourkia, N.; Lashgari, H.R. The microstructure, hardness and tensile properties of a new super high strength aluminum alloy with Zr addition. *Mater. Des.* **2010**, *31*, 4450–4456. [[CrossRef](#)]
28. Witte, F.; Hort, N.; Vogt, C.; Cohen, S.; Kainer, K.U.; Willumeit, R.; Feyerabend, F. Degradable biomaterials based on magnesium corrosion. *Curr. Opin. Solid St. M.* **2008**, *12*, 63–72. [[CrossRef](#)]
29. Saha, P.; Viswanathan, S. Engineering an Efficient Zirconium-Based Grain Refiner for Magnesium Alloys. *Int. J. Metalcast.* **2010**, *4*, 70–71. [[CrossRef](#)]
30. Li, H.; Li, Z.; Liu, Y.; Jiang, H. Effect of zirconium on the microstructure and mechanical properties of Zn-4%Al hypoeutectic alloy. *J. Alloys Compd.* **2014**, *592*, 127–134. [[CrossRef](#)]
31. Zhou, H.; Hou, R.; Yang, J.; Sheng, Y.; Li, Z.; Chen, L.; Li, W.; Wang, X. Influence of Zirconium (Zr) on the microstructure, mechanical properties and corrosion behavior of biodegradable zinc-magnesium alloys. *J. Alloys Compd.* **2020**, *840*, 155792. [[CrossRef](#)]
32. Wątroba, M.; Bednarczyk, W.; Kawałko, J.; Mech, K.; Marciszko, M.; Boelter, G.; Banzhaf, M.; Bała, P. Design of novel Zn-Ag-Zr alloy with enhanced strength as a potential biodegradable implant material. *Mater. Des.* **2019**, *183*, 108154. [[CrossRef](#)]
33. Jin, H.; Yang, L.; Lai, Y.; Liu, Y. The effects of Zr content and hot rolling on the microstructure and mechanical properties of Zn-1.5Cu-1.0Ag-xZr alloys. *J. Alloys Compd.* **2022**, *912*, 165116. [[CrossRef](#)]
34. Hua, X.; Wang, K.; Tong, X.; Lin, J. Microstructure, mechanical and corrosion properties of biodegradable Zn-Mg-Zr alloys for biomedical applications. *Mater. Lett.* **2022**, *323*, 132516. [[CrossRef](#)]
35. Ren, T.; Gao, X.; Xu, C.; Yang, L.; Guo, P.; Liu, H.; Chen, Y.; Sun, W.; Song, Z. Evaluation of as-extruded ternary Zn-Mg-Zr alloys for biomedical implantation material: In vitro and in vivo behavior. *Mater. Corros.* **2019**, *70*, 1056–1070. [[CrossRef](#)]
36. Martynenko, N.; Anisimova, N.; Rybalchenko, O.; Kiselevskiy, M.; Rybalchenko, G.; Tabachkova, N.; Zheleznyi, M.; Temralieva, D.; Bazhenov, V.; Koltygin, A.; et al. Structure, Biodegradation, and in vitro Bioactivity of Zn-1%Mg Alloy Strengthened by High-Pressure Torsion. *Materials* **2022**, *15*, 9073. [[CrossRef](#)]
37. ASTM G31-21. Standard Guide for Laboratory Immersion Corrosion Testing of Metals. ASTM International: West Conshohocken, PA, USA, 2004.

38. Martynenko, N.; Anisimova, N.; Rybalchenko, G.; Rybalchenko, O.; Serebryany, V.; Zheleznyi, M.; Shinkareva, M.; Gorbenko, A.; Temralieva, D.; Lukyanova, E.; et al. Effect of Rotary Swaging on Mechanical and Operational Properties of Zn–1%Mg and Zn–1%Mg–0.1%Ca Alloys. *Metals* **2023**, *13*, 1386. [CrossRef]
39. Zhen, Z.; Liu, X.; Huang, T.; Xi, T.; Zheng, Y. Hemolysis and cytotoxicity mechanisms of biodegradable magnesium and its alloys. *Mater. Sci. Eng. C Mater. Biol. Appl.* **2015**, *46*, 202–206. [CrossRef]
40. Zhao, R.; Ma, Q.; Zhang, L.; Zhang, J.; Xu, C.; Wu, Y.; Zhang, J. Revealing the influence of Zr micro-alloying and hot extrusion on a novel high ductility Zn–1Mg alloy. *Mater. Sci. Eng. A* **2021**, *801*, 140395. [CrossRef]
41. Wątroba, M.; Bednarczyk, W.; Kawałko, J.; Bała, P. Effect of zirconium microaddition on the microstructure and mechanical properties of Zn–Zr alloys. *Mater. Charact.* **2018**, *142*, 187–194. [CrossRef]
42. Peng, J.; Zhang, Z.; Liu, Z.; Li, Y.; Guo, P.; Zhou, W.; Wu, Y. The effect of texture and grain size on improving the mechanical properties of Mg–Al–Zn alloys by friction stir processing. *Sci. Rep.* **2018**, *8*, 4196. [CrossRef] [PubMed]
43. Guan, L.; Tang, G.; Chu, P.K.; Jiang, Y. Enhancement of ductility in Mg–3Al–1Zn alloy with tilted basal texture by electropulsing. *J. Mater. Res.* **2009**, *24*, 3674–3679. [CrossRef]
44. Straumal, B.; Martynenko, N.; Temralieva, D.; Serebryany, V.; Tabachkova, N.; Shchetinin, I.; Anisimova, N.; Kiselevskiy, M.; Kolyanova, A.; Raab, G.; et al. The Effect of Equal-Channel Angular Pressing on Microstructure, Mechanical Properties, and Biodegradation Behavior of Magnesium Alloyed with Silver and Gadolinium. *Crystals* **2020**, *10*, 918. [CrossRef]
45. Xu, Z.; Liu, H.; Hu, G.; Zhuo, X.; Yan, K.; Ju, J.; Wang, W.; Teng, H.; Jiang, J.; Bai, J. Developing Zn–1.5Mg Alloy with Simultaneous Improved Strength, Ductility and Suitable Biodegradability by Rolling at Room Temperature. *Acta Metall. Sin. (Engl. Lett.)* **2023**, *1*–11. [CrossRef]
46. Dvorský, D.; Kubásek, J.; Čapek, J.; Pinc, J.; Vojtěch, D. Characterization of Zn–1.5Mg and Zn–1.5Mg–0.5Ca Alloys Considered for Biomedical Application. *Key Eng. Mater.* **2019**, *821*, 17–22. [CrossRef]
47. Kubásek, J.; Vojtěch, D.; Pospíšilová, I.; Michalčová, A.; Maixner, J. Microstructure and mechanical properties of the micrograined hypoeutectic Zn–Mg alloy. *Int. J. Miner. Metall. Mater.* **2016**, *23*, 1167–1176. [CrossRef]
48. Vojtěch, D.; Kubásek, J.; Čapek, J.; Pospíšilová, I. Comparative mechanical and corrosion studies on magnesium, zinc and iron alloys as biodegradable metals. *Mater. Technol.* **2015**, *49*, 877–882. [CrossRef]
49. Liu, H.; Huang, H.; Zhang, Y.; Xu, Y.; Wang, C.; Sun, J.; Jiang, J.; Ma, A.; Xue, F.; Bai, J. Evolution of Mg–Zn second phases during ECAP at different processing temperatures and its impact on mechanical properties of Zn–1.6Mg (wt.%) alloys. *J. Alloys Compd.* **2019**, *811*, 151987. [CrossRef]
50. Huang, H.; Liu, H.; Wang, L.S.; Li, Y.-H.; Agbedor, S.-O.; Bai, J.; Xue, F.; Jiang, J.-H. A High-Strength and Biodegradable Zn–Mg Alloy with Refined Ternary Eutectic Structure Processed by ECAP. *Acta Metall. Sin. (Engl. Lett.)* **2020**, *33*, 1191–1200. [CrossRef]
51. Kafri, A.; Ovadia, S.; Goldman, J.; Drelich, J.; Aghion, E. The Suitability of Zn–1.3%Fe Alloy as a Biodegradable Implant Material. *Metals* **2018**, *8*, 153. [CrossRef]
52. Hammam, R.E.; Abdel-Gawad, S.A.; Moussa, M.E.; Shoeib, M.; El-Hadad, S. Study of Microstructure and Corrosion Behavior of Cast Zn–Al–Mg Alloys. *Inter. Metalcast.* **2023**, *17*, 2794–2807. [CrossRef]
53. Chen, K.; Lu, Y.; Tang, H.; Gao, Y.; Zhao, F.; Gu, X.; Fan, Y. Effect of strain on degradation behaviors of WE43, Fe and Zn wires. *Acta Biomater.* **2020**, *113*, 627–645. [CrossRef] [PubMed]
54. Wei, B.; Legut, D.; Sun, S.; Wang, H.T.; Shi, Z.Z.; Zhang, H.J.; Zhang, R.F. Synergistic effect of solute and strain on the electrochemical degradation in representative Zn-based and Mg-based alloys. *Corr. Sci.* **2021**, *188*, 109539. [CrossRef]
55. Krieg, R.; Vimalanandan, A.; Rohwerder, M. Corrosion of Zinc and Zn–Mg Alloys with Varying Microstructures and Magnesium Contents. *J. Electrochem. Soc.* **2014**, *161*, C156–C161. [CrossRef]
56. Liu, M.; Qiu, D.; Zhao, M.C.; Song, G.; Atrens, A. The effect of crystallographic orientation on the active corrosion of pure magnesium. *Scr. Mater.* **2008**, *58*, 421–424. [CrossRef]
57. Song, G.L.; Mishra, R.; Xu, Z. Crystallographic orientation and electrochemical activity of AZ31 Mg alloy. *Electrochem. Commun.* **2010**, *12*, 1009–1012. [CrossRef]
58. Jiang, J.; Huang, H.; Niu, J.; Zhu, D.; Yuan, G. Fabrication and characterization of biodegradable Zn–Cu–Mn alloy micro-tubes and vascular stents: Microstructure, texture, mechanical properties and corrosion behavior. *Acta Biomater.* **2022**, *151*, 647–660. [CrossRef]
59. Guillory, R.J.; Mostaed, E.; Oliver, A.A.; Morath, L.M.; Earley, E.J.; Flom, K.L.; Kolesar, T.M.; Mostaed, A.; Summers, H.D.; Kwesiga, M.P.; et al. Improved biocompatibility of Zn–Ag-based stent materials by microstructure refinement. *Acta Biomater.* **2022**, *145*, 416–426. [CrossRef]
60. Sahu, M.R.; Kumar, T.S.S.; Chakkingal, U. A review on recent advancements in biodegradable Mg–Ca alloys. *J. Magnes. Alloy.* **2022**, *10*, 2094–2117. [CrossRef]
61. Venezuela, J.; Dargusch, M.S. The influence of alloying and fabrication techniques on the mechanical properties, biodegradability and biocompatibility of zinc: A comprehensive review. *Acta Biomater.* **2019**, *87*, 1–40. [CrossRef]
62. Martynenko, N.; Lukyanova, E.; Anisimova, N.; Kiselevskiy, M.; Serebryany, V.; Yurchenko, N.; Raab, G.; Birbilis, N.; Salishchev, G.; Dobatkin, S.; et al. Improving the property profile of a bioresorbable Mg–Y–Nd–Zr alloy by deformation treatments. *Materialia* **2020**, *13*, 100841. [CrossRef]
63. Ma, J.; Zhao, N.; Zhu, D. Bioabsorbable zinc ion induced biphasic cellular responses in vascular smooth muscle cells. *Sci. Rep.* **2016**, *6*, 26661. [CrossRef] [PubMed]

64. Yang, H.; Qu, X.; Lin, W.; Chen, D.; Zhu, D.; Dai, K.; Zheng, Y. Enhanced osseointegration of Zn-Mg composites by tuning the release of Zn ions with sacrificial Mg-rich anode design. *ACS Biomater. Sci. Eng.* **2018**, *5*, 453–467. [[CrossRef](#)] [[PubMed](#)]
65. Jun, M.A.; Nan, Z.; Zhu, D. Endothelial cellular responses to biodegradable metal zinc. *ACS Biomater. Sci. Eng.* **2015**, *1*, 1174–1182.

Disclaimer/Publisher's Note: The statements, opinions and data contained in all publications are solely those of the individual author(s) and contributor(s) and not of MDPI and/or the editor(s). MDPI and/or the editor(s) disclaim responsibility for any injury to people or property resulting from any ideas, methods, instructions or products referred to in the content.